CrossMark

JፙM PAPERS

Role of surfactant-induced Marangoni stresses in retracting liquid sheets

C.R. Constante-Amores[1,2], J. Chergui[3], S. Shin[4], D. Juric[3,5], J.R. Castrejón-Pita[6,7] and A.A. Castrejón-Pita[1],†

[1]Department of Engineering Science, University of Oxford, Oxford OX1 3PJ, UK

[2]Mathematical Institute, University of Oxford, Oxford OX2 6GG, UK

[3]Université Paris Saclay, Centre National de la Recherche Scientifique (CNRS), Laboratoire Interdisciplinaire des Sciences du Numérique (LISN), 91400 Orsay, France

[4]Department of Mechanical and System Design Engineering, Hongik University, South Korea

[5]Department of Applied Mathematics and Theoretical Physics, University of Cambridge, Cambridge CB3 0WA, UK

[6]School of Engineering and Material Science, Queen Mary University of London, Mile End Road, London E1 4NS, UK

[7]Department of Mechanical Engineering, University College London, London WC1E 7JE, UK

In this work, we study the effect of insoluble surfactants on the three-dimensional rim-driven retraction dynamics of thin water sheets in air. We employ an interface-tracking/level-set method to ensure the full coupling between the surfactant-induced Marangoni stresses, interfacial diffusion and inertia. Our findings are contrasted with the (Newtonian) dynamics of a liquid sheet edge, finding that the surfactant concentration can delay, or effectively prevent, the breakup of the rim. Our simulations use the fastest growing Rayleigh–Plateau instability to drive droplet detachment from the fluid sheet (rim). The results of this work unravel the significant role of Marangoni stresses in the retracting sheet dynamics at large elasticity numbers. We study the sensitivity of the dynamics to the elasticity number and the rigidification of the interface.

1. Introduction

The capillary breakup of liquid films into droplets plays a major role in various unsteady fluid fragmentation phenomena, such as atomisation or droplet splashing

† Email address for correspondence: alfonso.castrejon-pita@wadham.ox.ac.uk

949 A32-1

(Villermaux 2020). It is therefore unsurprising that the sheet retraction dynamics has received significant interest since the initial experimental observations by Dupre (1867) and Rayleigh (1879). Capillary film retraction follows the puncturing of a static liquid film, where a capillary-induced flow drives the opening of the interface (a hole) at a constant speed, i.e. the Taylor–Culick velocity (Taylor 1959; Culick 1960). Early pictures by Rayleigh (1891) and Ranz (1959) show that the opening of the sheet results in the formation of a rim with roughly cylindrical caps, as the film moves away from the puncture. The desire to understand the fundamental mechanism underlying the development of the hole-driven expansion has led to numerous studies in this field, see for instance Debrégeas, Martin & Brochard-Wyart (1995); Keller, King & Ting (1995); Brenner & Gueyffier (1999); Fullana & Zaleski (1999); Sünderhauf, Raszillier & Durst (2002); Roisman, Horvat & Tropea (2006); Savva & Bush (2009); Krechetnikov (2010); Gordillo *et al.* (2011); Lhuissier & Villermaux (2011); Villermaux & Bossa (2011) and Agbaglah, Josserand & Zaleski (2013); Agbaglah (2021). Debrégeas *et al.* (1995) and Savva & Bush (2009) concluded that the retracting dynamics of a liquid sheet is governed by a balance between inertial, viscous and surface-tension forces. Accordingly, the Ohnesorge number, *Oh*, (i.e. ratio of viscous to capillary forces) becomes the most appropriate parameter to parametrise the flow dynamics. Different regimes have been identified that depend on *Oh*: (i) in the *Oh* < 1 regime, which is characterised by a nearly inviscid flow, the dynamics is driven by surface tension, leading to the formation of capillary waves ahead of the roughly cylindrical rim; (ii) in the *Oh* > 10 regime, viscous forces dominate the dynamics causing the suppression of the rim; and (iii) an intermediate regime bridges the two previous regimes.

The ground-breaking experiments of McEntee & Mysels (1969) proposed that a surface instability along the rim drives the formation of ligaments, and eventually, the ejection of droplets. Several studies have suggested that different physical mechanisms prompt the detachment of these droplets: a Rayleigh–Plateau (RP) instability (discussed below), a nonlinear amplification mechanism (Yarin & Weiss 1995), a Richtmyer–Meshkov instability and a competition/collaboration between the Richtmyer–Meshkov and Rayleigh–Taylor (RT) instabilities (Krechetnikov 2010).

However, Bremond & Villermaux (2006) (for the fragmentation of the lamella of colliding jets), Rieber & Frohn (1999) and Zhang *et al.* (2010) (for the fragmentation of the sheet crown from impacts of drops onto a thin layer of liquid) concluded that the RP instability is responsible for the onset of drop detachment. These findings contrast with the previous study by Fullana & Zaleski (1999), that suggests that the growth of the rim during the retraction prevents the onset of a RP instability. Finally, Agbaglah *et al.* (2013) (for a numerical sheet retraction in a frame of reference moving at the Taylor–Culick velocity) and Wang *et al.* (2018) (for drop impact onto a solid surface) showed that both the RT and RP instabilities are responsible for droplet generation from the rim. The former is important at early times during the deceleration of the ejected sheet, whereas the latter is predominant at longer times once the rim has already formed. According to recent studies by Wang & Bourouiba (2018, 2021), the ligament dynamics can result in end pinching, break up into satellite droplets or recombination into a single fluid volume.

McEntee & Mysels (1969) used surfactants in their experimental work to study the bursting of liquid films without directly endorsing the effects of Marangoni-induced flows. In contrast, recent studies have demonstrated the crucial role of surfactants on the dynamics of the capillary singularity (Ambravaneswaran, Phillips & Basaran 2000; Craster, Matar & Papageorgiou 2002; Timmermans & Lister 2002; Liao, Franses & Basaran 2006; Kamat *et al.* 2018). Constante-Amores *et al.* (2020) and Kamat *et al.* (2020)

showed that surfactant-induced Marangoni stresses inhibit end pinching for retracting liquid threads via the suppression of stagnation points, which in turn leads to flow reversal near the vicinity of the neck.

Three-dimensional numerical simulations of retracting liquid sheets are scarce in the literature due to the need for large aspect ratios to induce both the growth of instabilities at the rim, and the development of the nonlinear flow dynamics. In this work, the role of surfactant-induced Marangoni stresses on the retraction of thin liquid sheets and the detachment of droplets is studied in a three-dimensional, nonlinear framework. This paper is structured as follows: § 2 introduces the numerical method, governing dimensionless parameters, problem configuration and validation; § 3 provides the results from the simulations; and concluding remarks are given in § 4.

2. Problem formulation and numerical method

Numerical simulations were performed by solving the transient two-phase Navier–Stokes equations in a three-dimensional Cartesian domain $\boldsymbol{x} = (x, y, z)$ (see figure 1). The interface is captured via a hybrid front-tracking/level-set method and a convective–diffusion equation is solved for the surfactant transport along the deforming interface (Shin *et al.* 2018). All variables are made dimensionless following:

$$\tilde{x} = \frac{x}{h_0}, \quad \tilde{t} = \frac{t}{t_{inv}}, \quad \tilde{\boldsymbol{u}} = \frac{\boldsymbol{u}}{u_{TC}}, \quad \tilde{p} = \frac{p}{\rho_l u_{TC}^2}, \quad \tilde{\sigma} = \frac{\sigma}{\sigma_s}, \quad \tilde{\Gamma} = \frac{\Gamma}{\Gamma_\infty}, \qquad (2.1a\text{–}f)$$

where, t, $\boldsymbol{u}$ and p stand for time, velocity and pressure, respectively. The physical parameters correspond to the liquid density ρ_l, viscosity μ_l, surface tension σ, surfactant-free surface tension σ_s and $u_{TC} = \sqrt{2\sigma_s/(\rho h_0)}$, is the well-known Taylor–Culick speed; here, h_0 stands for the sheet thickness. In this study we focus on the low-*Oh* regime; hence, the characteristic time scale is given by the capillary time $t_{inv} = h_0/u_{TC} = \sqrt{\rho_l h_0^3/(2\sigma_s)}$. As seen, the interfacial surfactant concentration, Γ, is also made dimensionless through the saturation interfacial concentration, Γ_∞. As a result of the scaling in (2.1*a–f*), the dimensionless forms of the governing equations for the flow and the surfactant transport are respectively expressed as

$$\nabla \cdot \tilde{\boldsymbol{u}} = 0, \qquad (2.2)$$

$$\tilde{\rho} \left(\frac{\partial \tilde{\boldsymbol{u}}}{\partial \tilde{t}} + \tilde{\boldsymbol{u}} \cdot \nabla \tilde{\boldsymbol{u}} \right) + \nabla \tilde{p} = Oh \, \nabla \cdot \left[\tilde{\mu} (\nabla \tilde{\boldsymbol{u}} + \nabla \tilde{\boldsymbol{u}}^{\mathrm{T}}) \right] + \int_{\tilde{A}(\tilde{t})} (\tilde{\sigma} \tilde{\kappa} \boldsymbol{n} + \nabla_s \tilde{\sigma}) \, \delta \left(\tilde{\boldsymbol{x}} - \tilde{\boldsymbol{x}}_f \right) \, \mathrm{d}\tilde{A}, \qquad (2.3)$$

$$\frac{\partial \tilde{\Gamma}}{\partial \tilde{t}} + \nabla_s \cdot (\tilde{\Gamma} \tilde{\boldsymbol{u}}_{\mathrm{t}}) = \frac{1}{Pe_s} \nabla_s^2 \tilde{\Gamma}, \qquad (2.4)$$

which correspond to the equations of mass and momentum conservation and the convective–diffusion equations for the interfacial concentration, respectively. Here, the density $\tilde{\rho}$ and viscosity $\tilde{\mu}$ are defined by $\tilde{\rho} = \rho_g/\rho_l + (1 - \rho_g/\rho_l)\mathcal{H}(\tilde{\boldsymbol{x}}, \tilde{t})$ and $\tilde{\mu} = \mu_g/\mu_l + (1 - \mu_g/\mu_l)\mathcal{H}(\tilde{\boldsymbol{x}}, \tilde{t})$ wherein $\mathcal{H}(\tilde{\boldsymbol{x}}, \tilde{t})$ represents a smoothed Heaviside function. In this work, $\mathcal{H}(\tilde{\boldsymbol{x}}, \tilde{t})$ is zero in the gas phase and unity in the liquid. The subscript g designates the gas phase, $\tilde{\boldsymbol{u}}_t = (\tilde{\boldsymbol{u}}_s \cdot \boldsymbol{t})\boldsymbol{t}$ stands for the velocity vector tangential to the interface in which $\tilde{\boldsymbol{u}}_s$ corresponds to the interfacial velocity, κ stands for the interfacial curvature obtained from the Lagrangian interface structure and
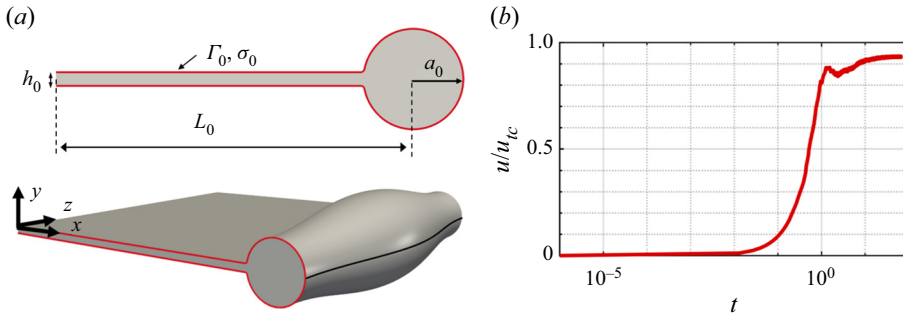
Figure 1. (*a*) Schematic view of the sheet and rim geometry: the initial shape of the retracting sheet (not to scale) is characterised by a cylindrical rim with $e = 0.2$ and an initial instability amplitude of $\epsilon = 0.25$. The black line represents the arclength, s, across the x–z plane ($y = \lambda/2$). (*b*) Presents the numerical results for the retraction velocity in terms of the Taylor–Culick value u_{TC} for a surfactant-free liquid sheet with $Oh = 0.1$, $\epsilon = 0$ and $e = 2$.

$\nabla_s = (\mathbf{I} - \mathbf{nn}) \cdot \nabla$ stands for the surface gradient operator wherein $\mathbf{I}$ is the identity tensor and $\mathbf{n}$ is the outward-pointing unit normal to the interface. Finally, $\tilde{\mathbf{x}}_f$ is the parameterisation of the interface $\tilde{A}(\tilde{t})$, and δ represents a Dirac delta function that is non-zero when $\tilde{\mathbf{x}} = \tilde{\mathbf{x}}_f$ only.

The dimensionless groups that govern the dynamics are defined as

$$Oh = \frac{\mu_l}{\sqrt{\sigma_s h_0 \rho_l}}, \quad Pe_s = \frac{u_{TC} h_0}{D_s}, \quad \beta_s = \frac{ReT\Gamma_\infty}{\sigma_s}, \qquad (2.5a\text{–}c)$$

where Oh and Pe_s stand for the Ohnesorge and (interfacial) Péclet numbers, respectively, while β_s is the surfactant elasticity number which provides a measure of the sensitivity of σ to Γ; here, Re is the ideal gas constant value (Re $= 8.314 \, \text{J K}^{-1} \, \text{mol}^{-1}$), T denotes temperature and D_s stands for the diffusion coefficient. The nonlinear Langmuir equation expresses σ in terms of Γ, i.e. $\tilde{\sigma} = 1 + \beta_s \ln(1 - \tilde{\Gamma})$, and the Marangoni stress, $\tilde{\tau}$, is given as a function of $\tilde{\Gamma}$ as $\tilde{\tau} = \nabla_s \tilde{\sigma} \cdot \mathbf{t} = -\beta_s/(1 - \tilde{\Gamma})\nabla_s \tilde{\Gamma} \cdot \mathbf{t}$. Tildes are dropped henceforth.

We present a brief summary of the numerical method used in this study. The Navier–Stokes equations are solved by a finite volume method on a staggered grid (Harlow & Welch 1965). The computational domain is discretised by a fixed regular grid (i.e. Eulerian grid) and the spatial derivatives are approximated by standard centred difference discretisation, except for the nonlinear term, which makes use of a second-order essentially non-oscillatory scheme (Sussman, Smereka & Osher 1994). The interface is tracked explicitly by an additional Lagrangian grid by using the front-tracking method, and the interface is reconstructed by using the level contour reconstruction method Shin & Juric (2002, 2009). Communication between the Eulerian and Lagrangian grids (for the transfer of the geometric information of the interface) is done by using the discrete delta function and the immersed boundary method of Peskin (1977). The advection of the Lagrangian interface is done by integrating $\mathrm{d}\mathbf{x}_f/\mathrm{d}t = V$ with a second-order Runge–Kutta method, where V stands for the interfacial velocity which has been calculated by interpolation from the Eulerian velocity. The code is parallelised through an algebraic domain-decomposition technique and the communication between subdomains for data exchange is managed by the message passing interface protocol. More details of the numerical method used to solve the above equations is described in detail in Shin *et al.* (2018)

949 A32-4

2.1. *Numerical set-up and validation*

Figure 1(*a*) illustrates the geometry used in this study; we have initialised the sheet film dynamics using a linearly unstable configuration, as proposed by Agbaglah *et al.* (2013). Thus, we have considered a thin liquid sheet of thickness h_0, and initial length L_0, connected to a cylindrical rim of radius a_0. The initial shape of the rim is given by $a(\omega, \varepsilon) = a_0[1 + \varepsilon \cos(\omega z)]$, where ε and ω stand for the perturbation amplitude and the growth rate, respectively. The dispersion relation for the RP instability suggests that the largest growth rate, ω, is obtained for a wavenumber $k \sim 0.6970$, which corresponds to $\lambda_{max} = 2\pi/k = 9.016a_0$ (where λ_{max} is the most unstable wavelength). All simulations were run using an initial perturbation amplitude of $\varepsilon = 0.25$ with $k \sim 0.6970$, unless stated otherwise in the text. See the supplementary material (SM) available at https://doi.org/10.1017/jfm.2022.768 for further discussion regarding the selection of ε.

Additionally to the dimensionless flow parameters, the flow dynamics is also controlled by the ratio of the film thickness to the radius of the rim, i.e. $e = h_0/a_0$. In this study, we consider the zero acceleration limit, and $e = 0.2$, following the work by Agbaglah *et al.* (2013), where their stability analysis and dispersion relationship depended on the initial acceleration (see SM for additional information about the choice of e).

As the liquid sheet retracts, the thickness of the rim grows over time as the rim engulfs the sheet, e decreases and the rim deceleration vanishes, resulting in the rim dynamics being fully driven by the RP instability. Therefore, the flow dynamics depends on two competing time scales: the time scale given by the RP instability in the (spanwise) z-direction (T_{RP}), and the time scales of the rim growth (T_{ret}). The time scale of the action of surface tension and droplet detachment is given by the capillary time, $T_{RP} = \sqrt{\rho_l a_0^3/\sigma_s}$. On the other hand, mass conservation results in the scaling $a(\mathrm{d}a/\mathrm{d}t) \sim hu_{TC}$, leading to $T_{ret} = a/(\mathrm{d}a/\mathrm{d}t) \sim \sqrt{\rho_l a_0^4/(2\sigma_s h_0)}$; for $T_{RP} \ll T_{ret}$, then, the liquid sheet must satisfy $\sqrt{h_0/a_0} \ll 1$, as $a_0^2 \sim h_0 L_0$, which leads to the next condition $\sqrt[4]{h_0/L_0} \ll 1$ that is accomplished at very high aspect ratios (see Mirjalili, Chan & Mani (2018) for more details). Finally, we justify the initial sinusoidal perturbation by looking into the breakup time T_B as a function of $T_B = f(Oh, \varepsilon)$ (see expression 5 from Driessen *et al.* 2013); for $T_B = f(Oh, \varepsilon = 0.25) \sim T_{RP}$.

The computational domain corresponds to $6.75\lambda_{max} \times \lambda_{max} \times \lambda_{max}$ (i.e. $304.29h_0 \times 45.08h_0 \times 45.08h_0$) where the x-coordinate is aligned with the length of the sheet. The domain is sufficiently large in the streamwise direction to avoid the effect of artificial reflections from the boundary in this direction. The simulations are initialised with fluids at rest in the absence of gravity. The periodic boundary condition is imposed on all the variables in the (spanwise) z-direction of the domain. A no-penetration boundary condition is prescribed for the bottom and top domains. The domain is discretised with a regular cubic mesh of size $\Delta x = h_0/6$, ensuring that our numerical predictions are mesh independent; our results do not vary with decreasing grid size. Note that similar mesh sizes have been used in previous studies (Agbaglah 2021; Gordillo *et al.* 2011) for three- and two-dimensional simulations of surfactant-free retracting liquid sheets. Additionally, liquid volume and surfactant mass conservation are satisfied with errors of under 0.001 %. Extensive mesh studies for surface-tension-driven phenomena with the same numerical methodology have been presented in Constante-Amores *et al.* (2020,2021*c*, *a*). At the early stages of the simulation, capillary action drives the formation of a smooth cylindrical rim at the free end of the liquid sheet. After a short transient stage, the dynamics reaches the Taylor–Culick regime, characterised by a constant retraction velocity. Figure 1(*b*) contrasts

our numerical results against the expected Taylor–Culick retraction velocity for $Oh = 0.1$, $\epsilon = 0$ and $e = 2$.

As seen, the constant retraction velocity is $\sim 8\%$ smaller than the predicted Taylor–Culick velocity. This difference is consistent with the observations by Agbaglah (2021) and Song & Tryggvason (1999) and is explained by the large density and viscosity ratios. The retraction dynamics of a liquid thread and the nonlinear dynamics before pinch-off have been validated previously by Constante-Amores *et al.* (2020). We refer to Shin *et al.* (2018) for the accuracy of the surfactant equations.

2.2. *Parameters*

Our conditions assume a retracting water liquid sheet in air, i.e. $\rho_g/\rho_l = 1.2 \times 10^{-3}$ and $\mu_g/\mu_l = 0.018$, as in the previous works of Agbaglah *et al.* (2013) and Agbaglah (2021). We assume a thickness of a soap film of $h_0 = 2.0$ μm, i.e. $Oh = 0.0833$ (in agreement with Meister & Scheele 1969). The parameter β_s depends on Γ_∞ and therefore on the critical micelle concentration, i.e. $\Gamma_\infty \sim O(10^{-6})$ mol m^{-2} for NBD-PC (1-palmitoyl-2-12-[(7-nitro-2-1,3-benzoxadiazol-4-yl)amino]dodecanoyl-sn-glycero-3 -phosphocholine); thus, here, we explore the range of $0.1 < \beta_s < 0.5$. We have set $Pe_s = 10^2$ following Batchvarov *et al.* (2020), who suggested that the interfacial dynamics is weakly dependent on Pe_s beyond this value i.e. convective effects, driven by surface-tension gradients (Marangoni stresses), rather than surface diffusion, dominate the interfacial distribution of surfactant when $Pe_s > 10^2$. Hence, for a liquid sheet characterised by $h_0 = 2.0\,\mu$m, the relevant time scales are given by $T_{RP} \sim O(10^{-8})$ s, $T_{ret} \sim O(10^{-6})$ s and the Marangoni time scale, $T_\tau \sim \mu_l h_0/\Delta\sigma \sim O(10^{-8})$ s. Consequently, Marangoni stresses play a key role in the flow dynamics.

3. Results

We start the discussion of the results by presenting a phenomenological picture of the interfacial dynamics in a phase diagram in a $\beta_s - Oh$ space. This dynamics ranges from a nearly inviscid sheet ($Oh \sim 10^{-3}$) to typical soap films ($Oh \sim 10^{-1}$). Figure 2 shows the regime map in terms of the interfacial dynamics predicted from our numerical simulations. Our results show that two distinct regimes can be identified based on the outcome of the retracting dynamics. At low β_s and Oh, surfactant-driven Marangoni stresses do not promote the reopening of the adjacent sheet connected to the rim; thus, capillary waves result in the formation of a hole behind the rim. This hole grows in the spanwise direction and separates the rim from the sheet. In fact, this dynamics has previously been observed by Mirjalili *et al.* (2018) and Constante-Amores *et al.* (2021*b*). The rest of the β_s–Oh space is dominated by surfactant-induced Marangoni stresses which reopen the adjacent sheet to promote droplet detachment via RP instability. Below, we focus on this regime, and provide an extensive explanation of the interfacial dynamics.

The spatio-temporal interfacial dynamics for the surfactant-free case, with $Oh = 0.0833$, is shown in figure 3(*a–e*). As seen, the initial rim instability grows to develop nonlinearities that eventually lead to a capillary singularity (break up). At early stages of the simulation, the fluid is pulled from the rim to form an elongated ligament (see figure 3*c*). Over time, the ligament undergoes end pinching, where capillarity overcomes viscosity to form a bulbous end (see figure 3*d*) terminating in the breakup of a droplet (see figure 3*e*). The interfacial shape prior to the capillary singularity closely resembles experimental observations by Zhang *et al.* (2010) and Wang & Bourouiba (2018, 2021).
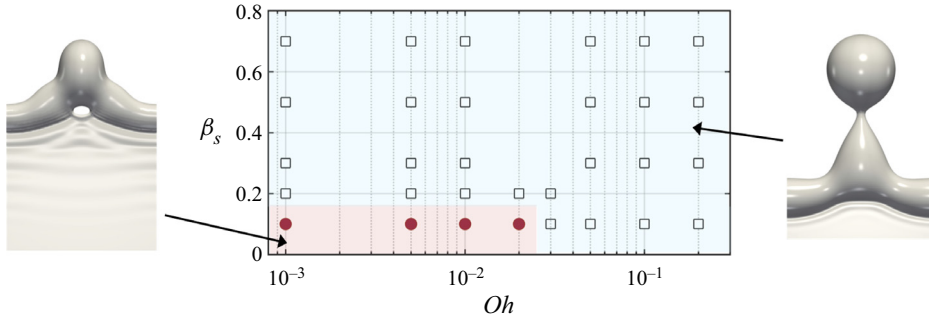
Figure 2. Regime map of the phenomenological interfacial dynamics in the β_s–Oh space. Circles represent numerical simulations in which capillary waves induce the formation of a hole behind the rim; hollow square symbols represent a droplet shedding from the rim via a RP instability. Here, $Pe_s = 100$, $\Gamma = \Gamma_\infty/2$, $e = 0.2$ and $\epsilon = 0.25$.

Additionally, we observe surface waves resulting from the development of capillary instabilities at the upstream of the rim.

Attention is now turned to the effect of surface-active agents by varying the surfactant elasticity parameter, β_s, with $Oh = 0.0833$, $Pe_s = 100$ and $\Gamma = \Gamma_\infty/2$. For $\beta_s = 0.1$, the spatio-temporal interfacial dynamics resembles that of a surfactant-free case, from the formation of the ligament to the eventual end pinching: the dynamics results in droplet shedding (see figure 3f–j). In this case, surfactant is accumulated at the base of the cylindrical rim as it gradually increases its size. Once the ligament is formed, τ induces a flow towards the ligament (see figure 3h) resulting in a longer ligament prior to pinch-off. However, as surfactant-induced Marangoni stresses are not sufficiently strong to evacuate Γ, the dynamics results in modest surfactant concentration gradients, and, in agreement with Constante-Amores *et al.* (2020), the ligaments break up. By increasing β_s, τ acts to reduce Γ gradients by inducing a flow from the rim towards the sheet, and from the rim towards the ligament (regions of low surfactant concentration), resulting in a severe reduction of the rim radius (displayed in figure 3). The surfactant-driven flow leads to the reopening of the fluid sheet adjacent to the retracting rim, thereby increasing its film thickness (see figure 4i); the Marangoni-induced flow also acts to suppress the capillary waves ahead of the rim (see figures 3(k–o) and 3(j–n) for $\beta_s = 0.3$ and $\beta_s = 0.5$, respectively).

We now turn our attention to the two-dimensional interfacial shape represented by Γ and spanwise Marangoni stresses, the tangential component of the surface velocity u_{t_z} and the streamwise surface velocity u_{t_x} (where the velocity is given in the reference frame of u_x at $z = 0$) presented in figure 4 at $t = 141.42$ and $t = 189.50$, respectively. As observed, the surfactant-driven flow, in the spanwise direction, results in the retardation of the dynamics brought about by surfactant-induced interfacial rigidification (see the dampening of u_{t_x} in the frame of difference in figure 4(b,f); as $\beta_s > 0$, $u_{t_x} < 0$). We observe that surfactant concentration gradients at $t = 141.42$ give rise to Marangoni stresses which drive a flow from the horizontal part of the rim towards the base of the ligament, and from the tip of the ligament to its base (for high β_s, the ligament tip has a nearly uniform distribution of Γ). The combined effect of Marangoni stresses is to bridge the surfactant gradient between the tip of the ligament and the rim (see figure 4h). This effect is sufficiently strong to promote the development of a thinner bulbous end, and cause a surfactant-driven escape from end pinching to a longer ligament (in agreement with Constante-Amores *et al.* (2020) and Kamat *et al.* (2020)). As expected, at a later stage, the nearly uniform distribution of surfactant concentration results in the elimination of Marangoni stresses
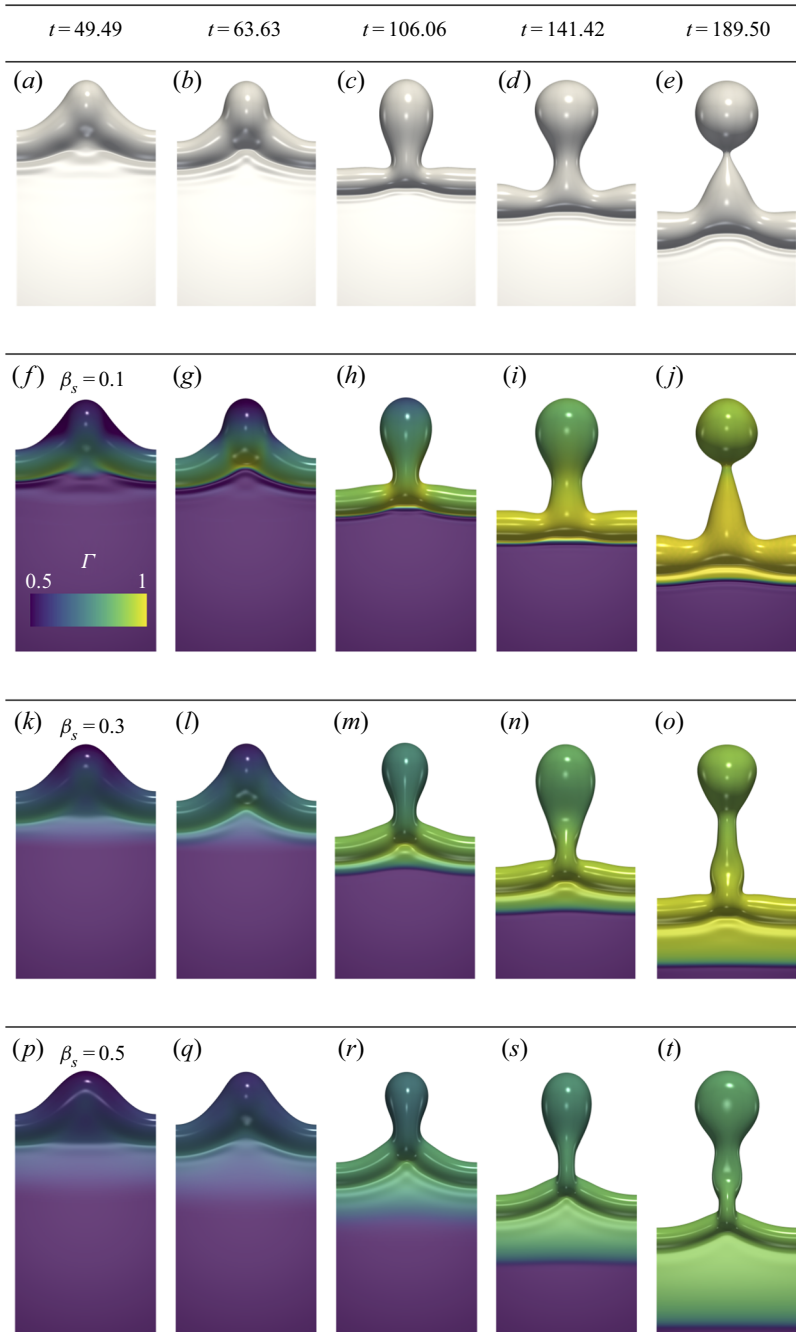
$t = 49.49$	$t = 63.63$	$t = 106.06$	$t = 141.42$	$t = 189.50$

Figure 3. Effect of surfactant elasticity (β_s) on the sheet retraction dynamics for insoluble surfactants. Here, the dimensionless parameters are $Oh = 0.0833$, $e = 0.2$ and $\epsilon = 0.25$; and for the surfactant-laden cases, $Pe_s = 100$ and $\Gamma = \Gamma_\infty/2$. For the surfactant-laden cases, the colour indicates the surfactant concentration Γ.

(see figure 4*h*). Figure 4(*c*,*g*) shows that $u_{t_z} > 0$ upstream and $u_{t_z} < 0$ downstream of the neck, i.e. a stagnation point is found in between. As the neck narrows, capillary-driven flow causes further neck thinning and the creation of a velocity maximum at u_{t_z}, as illustrated in figure 4(*c*,*g*), which is indicative of singularity formation. The u_{t_z} profile
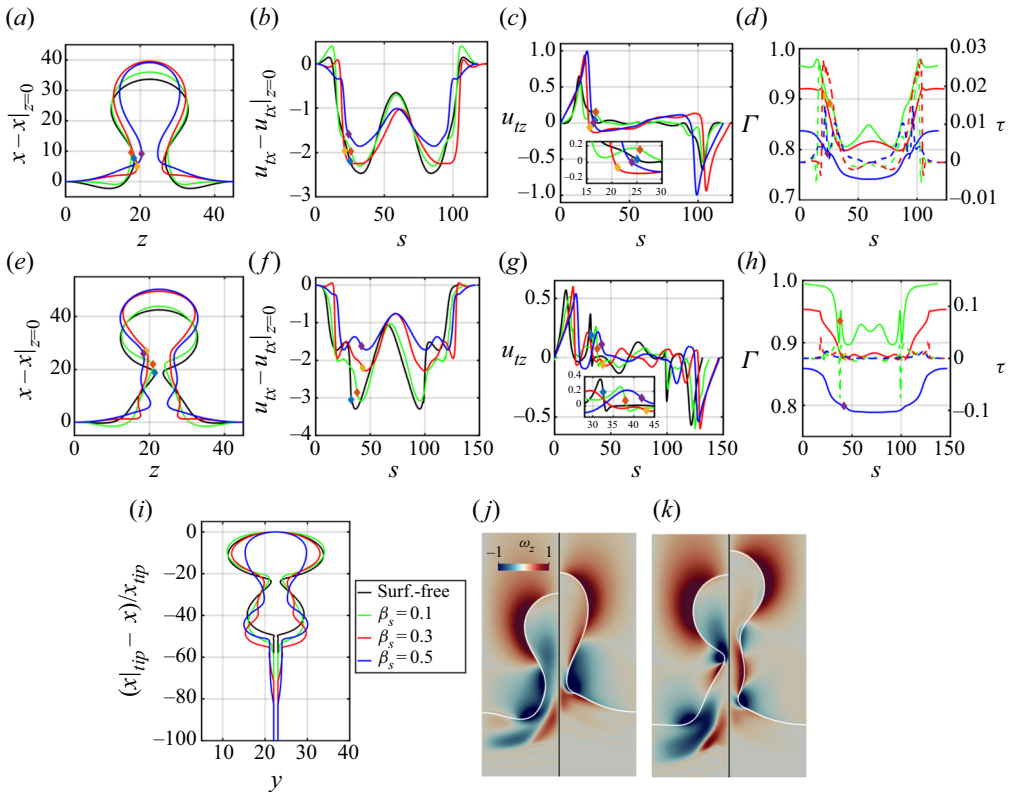
949 A32-8

Figure 4. Panels (*a–h*) show the effect of the elasticity parameter, β_s, on the flow and surfactant concentration during sheet retraction. Two-dimensional projection of the interface, Γ and τ and u_{tx} and u_{tz} in the x–z plane ($y = \lambda/2$) are shown in (*a–d*) and (*e–h*) for $t = 141.42$ and $t = 189.50$, respectively. Note that the abscissa in (*a,e*) corresponds to the z coordinate, and in (*b–d*) and (*f–h*) to the arclength, s. The diamond shapes show the location of the bulbous necks. Panel (*i*) shows the effect of β_s on the film thickness of the sheet in the x–y plane ($z = \lambda/2$). Panels (*j–k*) show the effect of surfactants on the vorticity, ω_z, for the surfactant-free case (left images), and the surfactant-laden case (right images), for $\beta_s = 0.5$ at $t = 141.42$ and $t = 189.50$, respectively.

for the surfactant-free case is characterised by the presence of a large velocity maximum and two stagnation points, with the neck located in between. By close inspection of the u_{t_z} profile of the surfactant-laden cases, it becomes clear that only one stagnation point is found near the neck for high β_s. The surfactant-induced Marangoni stresses result in the suppression of one of the stagnation points – in agreement with Constante-Amores *et al.* (2020, 2021*c*).

Figure 4(*j,k*) shows the vorticity field, i.e. $\omega = \nabla \times \boldsymbol{u}$, in terms of the interface location for the surfactant-free and surfactant-laden cases for $t = 141.42$ and $t = 189.50$ (the location is given in a reference frame where the rim position is found at $z = 0$). For all cases, a primary vortex (with a positive sign) is formed at the front region of the bulbous edge and is shed into the ambient fluid. For the surfactant-free case, we observe a negative vortex ring near the bulbous neck resulting from a change of curvature; this vortex ring grows over time, ending in breakup.

For the surfactant-laden case at $t = 141.42$, τ induces vorticity from the bulbous tip to the neck and from the rim to the ligament. This flow causes the neck to reopen; after escaping the singularity, the flow through the neck triggers the formation of a jet towards the centre of the bulbous region (these findings are consistent with
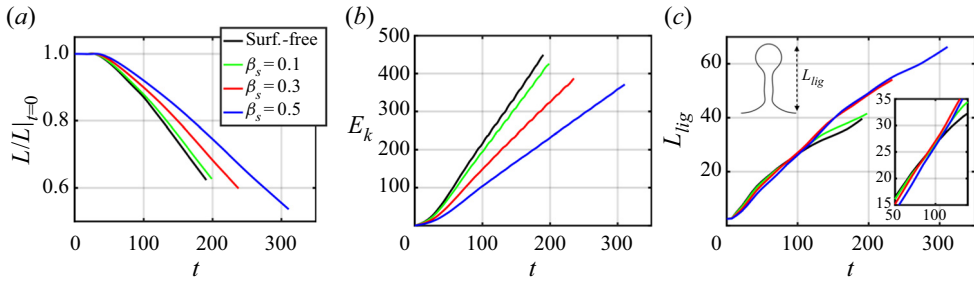
Figure 5. Temporal evolution of the ligament's tip position, the kinetic energy and the length of the ligament are shown in (*a–c*), respectively, for the surfactant-free and surfactant-laden cases. Simulations are stopped when the sheet sheds its first drop. All parameters remain unchanged from figure 3.

Constante-Amores *et al.* 2020). Additionally, the escape from pinch-off causes the length of the ligament to grow over time in the (*x*)-direction, forming a secondary bulbous and a secondary neck as well as a shift in the axial curvature signs (see figure 4*k*).

To provide conclusive evidence that Marangoni stresses drive the reopening of the neck, we run an additional simulation in which Marangoni stresses, or surface-tension gradients, are deactivated, i.e. $\nabla_s \sigma = 0$, to isolate the effects of a reduction in surface tension from those arising from Marangoni stresses. The Marangoni-suppressed case resembles the surfactant-free dynamics culminating in end pinching (see Supplementary animation). Additionally, we performed an additional surfactant-free simulation at the 'effective' Ohnesorge number, obtained by using the surface tension achieved by the surfactant, i.e. $Oh_{eff} = \mu / \sqrt{\rho h_0 \sigma_0} = 0.103$ (for $\beta_s = 0.5$ and $\Gamma_0 = 0.5$), finding similar results. Consequently, we claim Marangoni stresses are responsible of the change of the interfacial dynamics discussed above.

Finally, figure 5 shows the effect of the surfactant dynamics on the filament's tip location, L, the kinetic energy, $E_k = \int_{\mathcal{V}} (\rho \boldsymbol{u}^2)/2 \, d\mathcal{V}$, and the length of the ligament (defined from the tip of the bulbous edge to its rim). Here, the kinetic energy has been normalised by the surface energy $E_s = A_0 \sigma_s$, where A_0 is the initial surface of the sheet. The evidence for a surfactant-driven retardation of the dynamics can be seen by inspection of E_k and the streamwise location of the tip, which reveals that increasing β_s monotonically decreases the overall value of both E_k and L. Thus, the interfacial flow dynamics is retarded by Marangoni stresses resulting in a reduction in the retraction velocity. In figure 5(*c*), we report the length of the ligament until pinch-off, the addition of surfactant increases the ligament length prior to its breakup, becoming particularly pronounced at high β_s.

4. Concluding remarks

Results from three-dimensional numerical simulations of the retraction dynamics of thin liquid sheets in the presence of insoluble surfactants were presented. The liquid properties in the simulations were chosen to be consistent with a realistic air/water system, and the retraction velocity of the rim formed at the end is in good agreement with the Taylor–Culick speed. For the surfactant-laden cases, we have demonstrated that surfactant-induced Marangoni stresses drive a flow from the high surfactant concentration regions to the low concentration ones, reducing the kinetic energy, affecting the location of the bulbous tip and suppressing end pinching. With increasing elasticity number, the Marangoni stresses play a major role in the interfacial dynamics with the progressive elimination of the capillary wave structures upstream of the rim, where a complete

949 A32-10

interfacial rigidification is observed for large elasticity numbers. Additionally, Marangoni stresses drive flow towards the sheet, resulting in the reopening of the film thickness adjacent to the rim. Future research avenues are related to examining the role of solubility on the flow dynamics.

Author ORCIDs.

- C.R. Constante-Amores https://orcid.org/0000-0003-2476-5633;
- J. Chergui https://orcid.org/0000-0002-1578-6435;
- S. Shin https://orcid.org/0000-0002-9196-3966;
- D. Juric https://orcid.org/0000-0003-3703-0601;
- J.R. Castrejón-Pita https://orcid.org/0000-0001-8306-2095;
- A.A. Castrejón-Pita https://orcid.org/0000-0003-4995-2582.

REFERENCES

AGBAGLAH, G.G. 2021 Breakup of thin liquid sheets through hole–hole and hole–rim merging. *J. Fluid Mech.* **911**, A23.

AGBAGLAH, G., JOSSERAND, C. & ZALESKI, S. 2013 Longitudinal instability of a liquid rim. *Phys. Fluids* **25** (2), 022103.

AMBRAVANESWARAN, B., PHILLIPS, S.D. & BASARAN, O.A. 2000 Theoretical analysis of a dripping faucet. *Phys. Rev. Lett.* **85**, 5332–5335.

BATCHVAROV, A., KAHOUADJI, L., MAGNINI, M., CONSTANTE-AMORES, C.R., CRASTER, R.V., SHIN, S., CHERGUI, J., JURIC, D. & MATAR, O.K. 2020 Effect of surfactant on elongated bubbles in capillary tubes at high Reynolds number. *Phys. Rev. Fluids* **5**, 093605.

BREMOND, N. & VILLERMAUX, E. 2006 Atomization by jet impact. *J. Fluid Mech.* **549**, 273–306.

BRENNER, M.P. & GUEYFFIER, D. 1999 On the bursting of viscous films. *Phys. Fluids* **11** (3), 737–739.

CONSTANTE-AMORES, C.R., BATCHVAROV, A., KAHOUADJI, L., SHIN, S., CHERGUI, J., JURIC, D. & MATAR, O.K. 2021*a* Role of surfactant-induced Marangoni stresses in drop-interface coalescence. *J. Fluid Mech.* **925**, A15.

CONSTANTE-AMORES, C.R., KAHOUADJI, L., BATCHVAROV, A., SEUNGWON, S., CHERGUI, J., JURIC, D. & MATAR, O.K. 2020 Dynamics of retracting surfactant-laden ligaments at intermediate Ohnesorge number. *Phys. Rev. Fluids* **5**, 084007.

CONSTANTE-AMORES, C.R., KAHOUADJI, L., BATCHVAROV, A., SHIN, S., CHERGUI, J., JURIC, D. & MATAR, O.K. 2021*b* Direct numerical simulations of transient turbulent jets: vortex-interface interactions. *J. Fluid Mech.* **922**, A6.

CONSTANTE-AMORES, C.R., KAHOUADJI, L., BATCHVAROV, A., SHIN, S., CHERGUI, J., JURIC, D. & MATAR, O.K. 2021*c* Dynamics of a surfactant-laden bubble bursting through an interface. *J. Fluid Mech.* **911**, A57.

CRASTER, R.V., MATAR, O.K. & PAPAGEORGIOU, D.T. 2002 Pinchoff and satellite formation in surfactant covered viscous threads. *Phys. Fluids* **14** (4), 1364–1376.

CULICK, F.E.C. 1960 Comments on a ruptured soap film. *J. Appl. Phys.* **31**, 1128.

DEBRÉGEAS, G., MARTIN, P. & BROCHARD-WYART, F. 1995 Viscous bursting of suspended films. *Phys. Rev. Lett.* **75**, 3886.

DRIESSEN, T., JEURISSEN, R., WIJSHOFF, H., TOSCHI, F. & LOHSE, D. 2013 Stability of viscous long liquid filaments. *Phys. Fluids* **25** (6), 062109.

DUPRE, M.A. 1867 Sixieme memoire sur la theorie mechanique de la chaleur. *Ann. Chim. Phys.* **4** (11), 194–220.

FULLANA, J.M. & ZALESKI, S. 1999 Stability of a growing end rim in a liquid sheet of uniform thickness. *Phys. Fluids* **11**, 952.

GORDILLO, L., AGBAGLAH, G., DUCHEMIN, L. & JOSSERAND, C. 2011 Asymptotic behavior of a retracting two-dimensional fluid sheet. *Phys. Fluids* **23**, 122101.

HARLOW, F.H. & WELCH, J.E. 1965 Numerical calculation of time-dependent viscous incompressible flow of fluid with free surface. *Phys. Fluids* **8** (12), 2182–2189.

KAMAT, P.M., WAGONER, B.W., CASTREJÓN-PITA, A.A., CASTREJÓN-PITA, J.R., ANTHONY, C.R. & BASARAN, O.A. 2020 Surfactant-driven escape from endpinching during contraction of nearly inviscid filaments. *J. Fluid Mech.* **899**, A28.

KAMAT, P.M., WAGONER, B.W., THETE, S.S. & BASARAN, O.A. 2018 Role of marangoni stress during breakup of surfactant-covered liquid threads: reduced rates of thinning and microthread cascades. *Phys. Rev. Fluids* **3**, 043602.

KELLER, J.B., KING, A. & TING, L. 1995 Blob formation. *Phys. Fluids* **7**, 226.

KRECHETNIKOV, R. 2010 Stability of liquid sheet edges. *Phys. Fluids* **22**, 092101.

LHUISSIER, H. & VILLERMAUX, E. 2011 The destabilization of an initially thick liquid sheet edge. *Phys. Fluids* **23**, 091705.

LIAO, Y.C., FRANSES, E.I. & BASARAN, O.A. 2006 Deformation and breakup of a stretching liquid bridge covered with an insoluble surfactant monolayer. *Phys. Fluids* **18** (2), 022101.

MCENTEE, W.R. & MYSELS, K.J. 1969 Bursting of soap films. I. An experimental study. *J. Phys. Chem.* **73** (9), 3018–3028.

MEISTER, B.J. & SCHEELE, G.F. 1969 Prediction of jet length in immiscible liquid systems. *AIChE J.* **15** (5), 689–699.

MIRJALILI, S., CHAN, W.H.R. & MANI, A. 2018 High fidelity simulations of micro-bubble shedding from retracting thin gas films in the context of liquid–liquid impact. In *32nd Symposium on Naval Hydrodynamics*.

PESKIN, C.S. 1977 Numerical analysis of blood flow in the heart. *J. Comput. Phys.* **25** (3), 220–252.

RANZ, W.E. 1959 Some experiments on the dynamics of liquid films. *Intl J. Appl. Phys.* **30** (12), 1950–1955.

RAYLEIGH, LORD 1879 On the capillary phenomena of jets. *Proc. R. Soc. Lond.* **29**, 71–97.

RAYLEIGH, LORD 1891 Some applications of photography. *Nature* **44** (1133), 249–254.

RIEBER, M. & FROHN, A. 1999 A numerical study on the mechanism of splashing. *Intl J. Heat Fluid* **20** (5), 455–461.

ROISMAN, I.V., HORVAT, K. & TROPEA, C. 2006 Spray impact: rim transverse instability initiating fingering and splash, and description of a secondary spray. *Phys. Fluids* **18**, 102104.

SAVVA, N. & BUSH, J.W.M. 2009 Viscous sheet retraction. *J. Fluid Mech.* **626**, 211–240.

SHIN, S., CHERGUI, J. & JURIC, D. 2017 A solver for massively parallel direct numerical simulation of three-dimensional multiphase flows. *J. Mech. Sci. Technol.* **31**, 1739–1751.

SHIN, S., CHERGUI, J., JURIC, D., KAHOUADJI, L., MATAR, O.K. & CRASTER, R.V. 2018 A hybrid interface tracking – level set technique for multiphase flow with soluble surfactant. *J. Comput. Phys.* **359**, 409–435.

SHIN, S. & JURIC, D. 2002 Modeling three-dimensional multiphase flow using a level contour reconstruction method for front tracking without connectivity. *J. Comput. Phys.* **180**, 427–470.

SHIN, S. & JURIC, D. 2009 A hybrid interface method for three-dimensional multiphase flows based on front-tracking and level set techniques. *Intl J. Numer. Meth. Fluids* **60**, 753–778.

SONG, M. & TRYGGVASON, G. 1999 The formation of thick borders on an initially stationary fluid sheet. *Phys. Fluids* **11** (9), 2487–2493.

SÜNDERHAUF, G., RASZILLIER, H. & DURST, F. 2002 The retraction of the edge of a planar liquid sheet. *Phys. Fluids* **14**, 198.

SUSSMAN, M., SMEREKA, P. & OSHER, S. 1994 A level set approach for computing solutions to incompressible two-phase flow. *J. Comput. Phys.* **114** (1), 146–159.

TAYLOR, G.I. 1959 The dynamics of thin sheets of fluid. II. Waves on fluid sheets. *Proc. R. Soc. Lond.* A **253**, 296.

TIMMERMANS, M.-L.E. & LISTER, J.R. 2002 The effect of surfactant on the stability of a liquid thread. *J. Fluid Mech.* **459**, 289–306.

VILLERMAUX, E. 2020 Fragmentation versus cohesion. *J. Fluid Mech.* **898**, P1.

VILLERMAUX, E. & BOSSA, B. 2011 Drop fragmentation on impact. *J. Fluid Mech.* **668**, 412–435.

WANG, Y. & BOUROUIBA, L. 2018 Unsteady sheet fragmentation: droplet sizes and speeds. *J. Fluid Mech.* **848**, 946–967.

WANG, Y. & BOUROUIBA, L. 2021 Growth and breakup of ligaments in unsteady fragmentation. *J. Fluid Mech.* **910**, A39.

WANG, Y., DANDEKAR, R., BUSTOS, N., POULAIN, S. & BOUROUIBA, L. 2018 Universal rim thickness in unsteady sheet fragmentation. *Phys. Rev. Lett.* **120**, 204503.

YARIN, A.L. & WEISS, D.A. 1995 Impact of drops on solid surfaces: self-similar capillary waves, and splashing as a new type of kinematic discontinuity. *J. Fluid Mech.* **283**, 141–173.

ZHANG, L.V., BRUNET, P., EGGERS, J. & DEEGAN, R.D. 2010 Wavelength selection in the crown splash. *Phys. Fluids* **22**, 122105.